crystals

MDPI

Article

Gemstone Inclusion Study by 3D Raman-Mapping and High-Resolution X-ray Computed Tomography: The Case of Trapiche Emerald from Swat, Pakistan

Yujie Gao [1], Mingyue He [2,*], Xu Li [3], Moqing Lin [1], Xueying Sun [1] and Yanfang Zhang [4]

[1] Guild Gem Laboratories, Shenzhen 518020, China
[2] School of Gemology, China University of Geosciences, Beijing 100083, China
[3] The Testing and Technology Center for Industrial Product of Shenzhen Customs, Shenzhen 518067, China
[4] Tianjin Sanying Precision Instruments Co., Ltd., Tianjin 300399, China
* Correspondence: hemy@cugb.edu.cn

Abstract: Gemstones usually contain inclusions as the natural hallmark of their formation. Studies on inclusions may contribute to our understanding of the gem and better adapt to the gems and jewelry industry. In this study, we applied advanced 3D Raman mapping and high-resolution X-ray computed tomography (HRXCT) and conducted a thorough experiment on one emerald with a special trapiche pattern containing a colorless core, solid minerals, and fluids. Hematite and magnetite were identified as metallic minerals by the Raman spectrum. The hexagonal core is beryl, and the voids are primarily filled with CO_2 and N_2. HRXCT demonstrated a visualized distribution of these inclusions within the gem host by reconstructing a 3D illustration. Further calculation of the volume of inclusions regarding the host showed that the minerals take up 0.07%, void 0.03%, and the hexagonal core 8.25%. The combined application of Raman-Mapping and X-ray Micro Computed Tomography proved to be a very promising technique for tracing the gemstones by characterizing the unique inclusions (identification and morphology) within the gem host.

Keywords: gemstone; trapiche emerald; 3D Raman Mapping; high-resolution X-ray computed tomography (HRXCT); inclusions; hematite; magnetite; CO_2

check for updates

Citation: Gao, Y.; He, M.; Li, X.; Lin, M.; Sun, X.; Zhang, Y. Gemstone Inclusion Study by 3D Raman-Mapping and High-Resolution X-ray Computed Tomography: The Case of Trapiche Emerald from Swat, Pakistan. *Crystals* **2022**, *12*, 1829. https://doi.org/10.3390/cryst12121829

Academic Editor: Vladislav V. Gurzhiy

Received: 8 November 2022
Accepted: 5 December 2022
Published: 15 December 2022

Publisher's Note: MDPI stays neutral with regard to jurisdictional claims in published maps and institutional affiliations.

Copyright: © 2022 by the authors. Licensee MDPI, Basel, Switzerland. This article is an open access article distributed under the terms and conditions of the Creative Commons Attribution (CC BY) license (https://creativecommons.org/licenses/by/4.0/).

1. Introduction

Gemstones are usually highly valued and prominent in the trade owing to their beauty and rarity. The gem materials usually contain inclusions trapped during their formation. As the inclusions contain the message of the ancient earth, well-studied research may unveil nature's secret.

Furthermore, the inclusions, such as trapped mineral crystals, rock relics, and fluids, are unique to the gem host. Based on the phase, they are classified as solid, liquid, and gaseous. Minerals are the most commonly encountered, while the liquid and gaseous usually come together as two-phase inclusions, such as the negative crystal containing water and CO_2 in an emerald. Solid inclusions can be categorized into protogenetic, syngenetic, and epigenetic types inclusions based on the order in which they formed concerning their hosts [1]. A protogenetic inclusion refers to those forms before the gem host, i.e., older than the gem, such as calcite found in Burmese ruby [2] and mica found in Zambian emerald [3,4]. A syngenetic inclusion represents inclusions forming simultaneously with the host, meaning that the gem and inclusions are of the same age. Garnet and apatite were found as syngenetic inclusions in carbonado [5]. An epigenetic inclusion means inclusion forms after the host, meaning it is younger than the host. Gems usually contain open fissures owing to the unideal growth environment. Hence, the substance around the gem may go inside the cracks and stay within. Limonite is commonly encountered in Sri Lanka sapphire and partially heals the fracture of the host [6].

The Raman effect was first reported in 1928 [7]. Afterward, Raman spectroscopy was developed and applied to many fields, including gemology [8]. Micro-Raman spectroscopy has been applied to sapphires from various localities, and the mineral inclusions were successfully identified, such as anatase, rutile, and calcite [9]. Additionally, less common minerals can also be detected by Raman, such as palygorskite fibers in pink opals from Mexico and Peru [10] and diopside needles in demantoids from Russia [11]. More inclusion identification cases and related references can be detailed in previous literature [12,13].

The 3D mapping takes the Raman application to gemstones to a higher level, demonstrating the tiny difference in a specific selected area and presenting a much more visualized scene of the inclusion within the gem host. Eaton-Magaña and the co-authors have conducted the application of Raman mapping on gem materials such as diamonds [13]. Their experiment mainly focuses on the surface and the near-surface part, and the results are exciting and promising. In this research, we couple the Micro-Raman spectrometer with a 3D moving sample stage, enabling us to set the accurate position of the confocal laser beam and perform the mapping on the inclusions of selected samples.

Secondly, the confocal micro-Raman spectroscopy could identify the inclusion based on their unique spectral pattern. 3D mapping further scans the selected area of the inclusions and helps us understand the overall morphology of the inclusions and their relationship with the host in a three-dimensional way.

X-ray image techniques have been a promising newcomer since the 1990s [14] and have been widely applied to gemology, mainly in pearls and diamonds. Sunagawa et al. [15] used X-ray diffraction with cathodoluminescence to determine whether two faceted diamonds were cut from the same rough. Later research also demonstrated the application of an X-ray fingerprinting routine for cutting diamonds [16]. The X-ray has also been proven helpful in deciding whether pearls are natural or cultured and grown in saltwater or freshwater based on the details of their internal features [17,18].

HRXCT is a non-destructive method that combines the X-ray source and micro-objective coupled detector. It uses the comparison of X-ray attenuation on a series of continuous X-ray plates with different viewing angles to reconstruct the 3D distribution of regions of different densities in many materials. A review by Cnudde and Boone in 2013 demonstrated the high-resolution X-ray computed tomography applied to geoscience materials [19]. The in situ nature of gold particles and associated minerals can be characterized using high-resolution X-ray computed tomography and PVB analysis, which can reveal particle sizes, volumes, shapes, orientations, and textural relationships. This was demonstrated in a recent study on orogenic gold ores from Brazil [20].

The first brief report on the X-ray 3D applied on a gemstone was by Giuliani et al., who performed an X-ray 3D scanning on a demantoid and presented a clear result, revealing the internal morphology of the fluid and vapor within the cavity [21]. Furthermore, Richard et al. [22] performed high-resolution X-ray computed tomography (HRXCT) on the fluids and melted inclusions of several gemstone varieties. Their results showed that HRXCT is a promising tool for the non-destructive characterization of fluid and melt inclusions. Heyn et al. performed the X-ray CT on several gemstone varieties, including corundum, topaz, and quartz [23].

Usually, the standard microscopic observation under a gemological microscope equipped with various lighting conditions could reveal the inclusion scene and provide valuable information on the gemstone's variety, treatment, and origin. However, such a method is prohibited mainly if the stone is not polished or a faceted stone is set into metal as jewelry. The colored stones are collected as rough from underground and fashioned and polished into faceted or cabochon gemstones. The interior features are barely seen under a microscope if the stone is in a rough state with a raw surface, since the raw surface will diffuse the light, prohibiting it from being captured by the microscope. By comparison, X-ray micro-computed tomography can penetrate the bulk of the sample and avoid interference from the surface, enabling us to see the internal scene of the gemstone at a more accurate level.

The new application of advanced technology to the inclusion of gemstones can contribute to elevating the research level and advance our understanding of the formation and growth mechanism of the gemstone and the adaption of the inclusion in the gems and jewelry industry.

In this study, we demonstrate the capabilities of HRXCT by scanning a trapiche emerald with a distinctive growth pattern in three dimensions, displaying the form of fluid and mineral inclusions and recreating the overall volume and volumes of each phase using post-process software. Raman mapping and HRXCT recorded the experiment results performed on the trapiche emerald sample. The combined technique of 3D Raman mapping and HRXCT has proven to be quite valuable in furthering our understanding of the inclusions within a gemstone.

2. Materials and Methods

2.1. Materials

In this study, we have selected one trapiche-like emerald from Swat Valley, Pakistan, to demonstrate the combination of 3D Raman mapping and high-resolution X-ray computed tomography (HRXCT). Trapiche-like emeralds contain multiple inclusions, including minerals and fluids, which could serve as a good example to exhibit the high power of Raman and HRXCT. The chosen sample represents a trapiche-like growth pattern within emeralds, which can be seen in emeralds from Swat Valley, as shown in Figure 1. This chosen sample weighs 0.535 ct, with a size of 6.32 × 5.65 × 1.56 mm^3, and its trapiche pattern consists of minute black inclusions surrounding a colorless core, as shown in Figure 2.

Figure 1. Six emerald wafers from Swat, Pakistan show a trapiche-like pattern weighing from 0.53 ct to 0.83 ct, with a thickness of around 1.51 to 2.08 mm. We have chosen the fourth sample from the left to study its inclusion further.

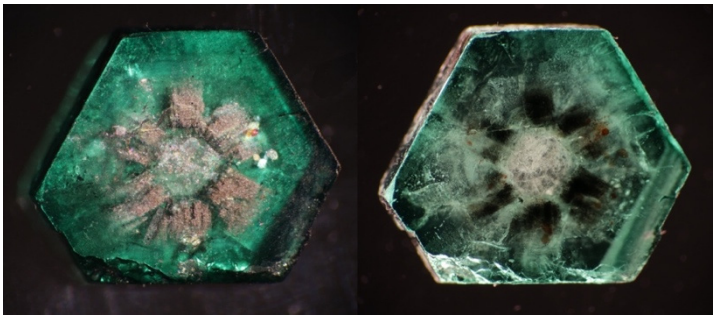

Figure 2. This chosen sample in this study, weighing 0.535 ct, with a size of 6.32 × 5.65 × 1.56 mm^3, shows a trapiche pattern consisting of a minute black inclusion surrounding a colorless core.

2.2. Methods

In this study, we have applied three methods to study the inclusions of a gemstone, including standard gemological microscopic observation, 3D Raman mapping, and high-resolution X-ray computed tomography (HRXCT).

2.2.1. Standard Gemology

Standard gemology combined with gemological microscopic observation allows for visual inspection of the inclusion under a well-equipped microscope and presents a broad scene of inclusion distribution. Inclusions were observed with an 80× magnification gemological microscope with S6D Leica optics equipped with different lighting sources, including transmitting light, reflective illumination, and oblique fibers.

2.2.2. Raman

The Horiba Xplora Plus Raman system (Horiba France SAS, Palaiseau, France) performed Raman micro-spectroscopy on the inclusions in this study. The machine was equipped with three lasers of 473 nm, 532 nm, and 783 nm. All the lasers were applied to the sample in this study to find the most prominent and effective one. As a result, we applied a 473 nm laser to the emerald sample. The spectra were recorded in the 400–2000 cm^{-1} range with a spectral resolution of 4 cm^{-1} and 8 scans at 7.5 kHz scanning speed.

Raman spectra were primarily collected in the range of 2000–100 cm^{-1}. The 3D Ram mapping was performed on a selected sample area coupled with an XYZ stage, which the software can automatically control. The site's position was chosen as a cube, with specific x, y, and z position values constrained within a particular range, with increments between 1 and 2 μm.

We randomly chose three plates of hematite and magnetite for Raman mapping, which could show the overall form and size in three dimensions. The mapping area is strictly measured by the *X*, *Y*, and *Z*-axis, determined by the XYZ sample stage, with accuracy as low as 0.1 μm. The XYZ parameters include the starting point, ending point, increment step, and the number of points along the axis, which can be seen in detail in Table 1. The 3D Raman mapping is pretty time-consuming, usually taking hours to acquire a decent result and half to one day to get a good one, depending on the quality of the finish spectrum and reconstructed images.

Table 1. The 3D Raman mapping parameters on the magnetite and hematite inclusions.

Parameters		Mag-02	Hem-02
X	Range/μm	(−15, 15.9)	(−17.5, 17.5)
	Step/μm	0.8	3.9
	Size	40	10
Y	Range/μm	(−9.7, 7)	(−23.1, 19.9)
	Step/μm	0.8	3.9
	Size	22	12
Z	Range/μm	(−5, 7)	(−100, 100)
	Step/μm	0.5	4
	Size	25	51
Total Volume/μm^3		6212.4	301,000
Total Time		36 h 30 min	14 h 21 min
Total Spectrum		22,000	6120

2.2.3. HRXCT

We applied nanoVoxel-3000 X-ray three-dimensional microscopy computerized tomography to analyze a 0.55 ct trapiche-like emerald from Swat Valley, Pakistan. We collected 1170 images by scanning them, layer by layer of the sample, within 90 min using the VoxelStudio Scan software V1.0 in Tianjin, China. The testing parameters include 60 kV voltage, 50 μA current, and 3.24 μm resolution. The post-processes are reconstructed based on the finished pictures by the VoxelStudio Recon software.

3. Results and Discussion

Trapiche emeralds from Colombia have been well-known in the gem trade. They were first described by the French mineralogist Emile Bertrand [24]. Pogue's study [25] showed the first mention of inclusions of carbonaceous substance in the emeralds "arranged in a six-rayed centering about a tapering hexagonal core". A recent study [26] showed an advanced understanding of the texture and growth mechanism of Colombian trapiche emeralds. Colombia was the only one producing trapiche emeralds until it was reported that the trapiche-pattern was also observed in emeralds from Swat Valley, Pakistan [27].

Unlike the Colombian counterpart, the Pakistan material was composed of four parts from rim to core: a green edge, a light green area, six black arms, and a colorless center,

as illustrated in Figure 3. The edges were a highly saturated green, and most were relatively clean except for several fractures and tiny fluid inclusions. The edges ranged from approximately 1 to 2 mm wide. Although the boundary between the green border and the light area was not very sharp, a hexagonal boundary was visible. Six black arms spread in a hexagonal symmetric pattern, with each arm perpendicular to the hexagonal side. The colorless core usually had a hexagonal shape.

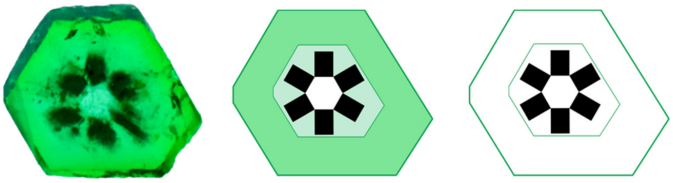

Figure 3. The illustration of the trapiche emerald in this study comprises four parts: green rim, light green color zoning, six black arms, and one nearly colorless hexagonal core.

As demonstrated in Figure 4, the image record from Micro-CT shows a general structure of the sample viewing from three angles along with a body view. This sample can be divided into four parts based on density: the emerald host, metallic minerals, voids, and the core. Figure 5 shows a clear boundary between the core and other parts, indicating a distinct difference in density. The metallic mineral shows a bright luster, and the voids exhibit black dots, which are indicated by red and blue circles, respectively, in Figure 5. The core exhibits a clear and well-formed hexagonal outline showing darker color.

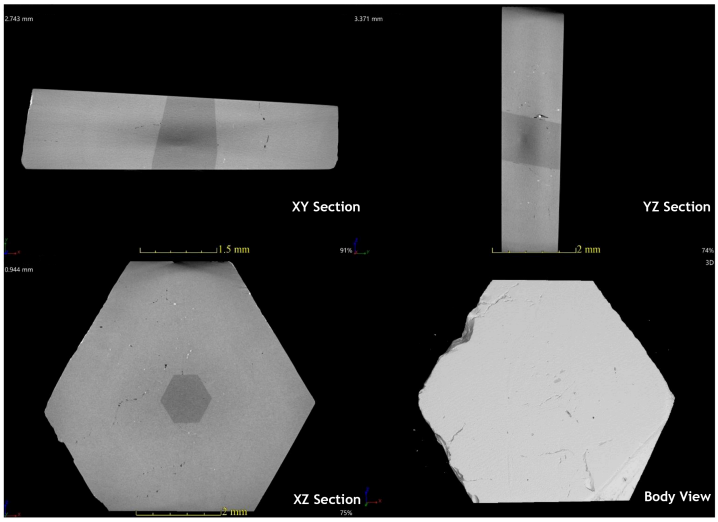

Figure 4. The inner structure of the gem can be observed from three different sections, and the three-dimensional structure of the sample can also be observed from the body view.

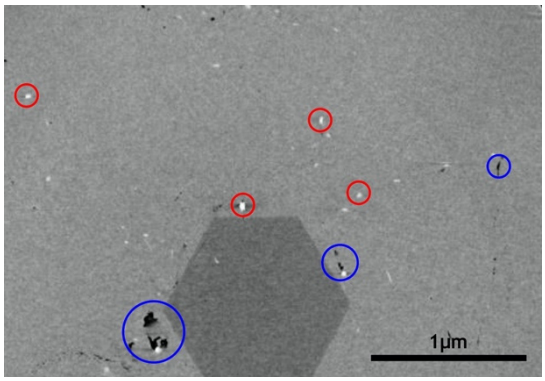

Figure 5. The HRXCT image shows the metal minerals (red circle) and voids (blue circle) in the sample, accompanied by a hexagonal core.

3.1. The Metallic Inclusions

Microscopic observation revealed metallic minerals, and the magnetite (Mag) concentrated in small size with a gray color in a systematic way. At the same time, the hematite (Hem) shows subhedral hexagonal growth habits showing bright interference color, as shown in Figure 6. Raman tests identify two mineral varieties as magnetite and hematite. An X-ray CT result showed that the metallic inclusions are scattered along with the gem host, and they take up about 0.07% by volume in total. We will demonstrate the results and discuss them separately.

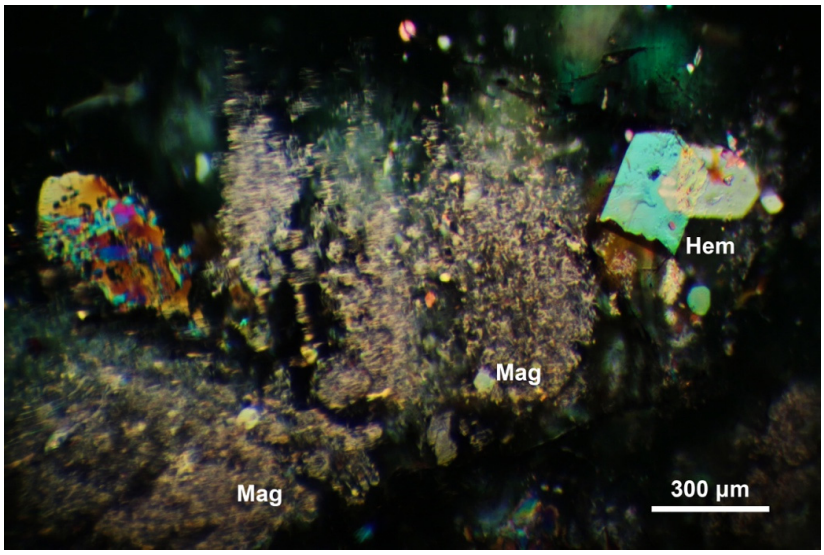

Figure 6. The metallic minerals were observed under microscopic observation, Mag: magnetite, Hem: hematite.

3.1.1. Magnetite

Magnetite is a commonly seen iron oxide mineral with a chemical formula of Fe_3O_4, belonging to the isotropic crystal system. In this study, the magnetite minerals within the emerald host appear black when observed by the naked eye. The well-distributed approach of magnetite gives rise to the trapiche pattern of the emerald host. Further observation under high magnification of the microscope showed that the magnetite is thin platy with a hexagonal outline, while some may exhibit a skeleton appearance. The typical reflective grey color is characteristic of magnetite, as shown in Figure 7.

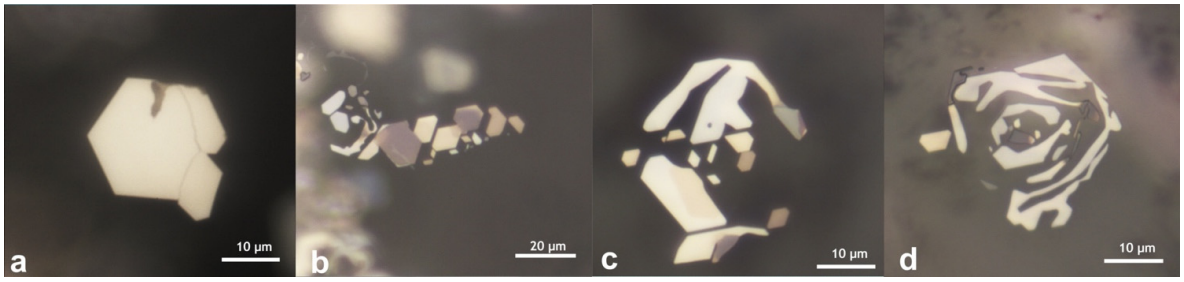

Figure 7. Magnetite shows a hexagonal shape (**a**,**b**) and sometimes a skeleton pattern (**c**,**d**).

Raman test reveals feature peaks at 661 and 534 cm^{-1}, which agrees with magnetite from the RRUFF online database, as shown in Figure 8. The prominent peak at 686 cm^{-1} and a weak peak at 399 cm^{-1} originate from the emerald host. No distinct magnetism was observed when we applied a magnet close to the emerald sample. 3D Raman mapping was conducted on one selected magnetite to study the morphology of the magnetite further. Figure 9 contains seven Raman spectra recorded on this chosen magnetite with a constant

z-axis value ranging from −5 µm to 3 µm with fixed x and y, as indicated by the legend. The intensity of the feature peak of magnetite at 661 cm^{-1} starts to increase as the Z value starts from −5 µm, and it became most distinct when z = −1 µm and decreased to nearly none at the z value moved to 3 µm.

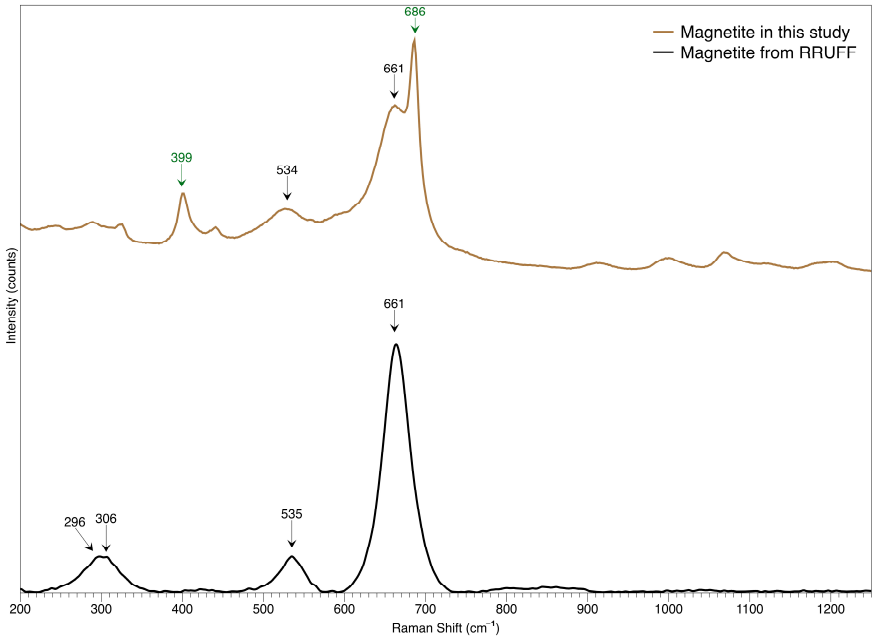

Figure 8. Raman spectrum analysis identifies these skeleton and grey platy inclusions as magnetite. Peaks at 661 and 535 cm^{-1} agree with two prominent peaks of magnetite, according to RRUFF online database, while peaks at 686 and 399 cm^{-1} may be assigned to the emerald host.

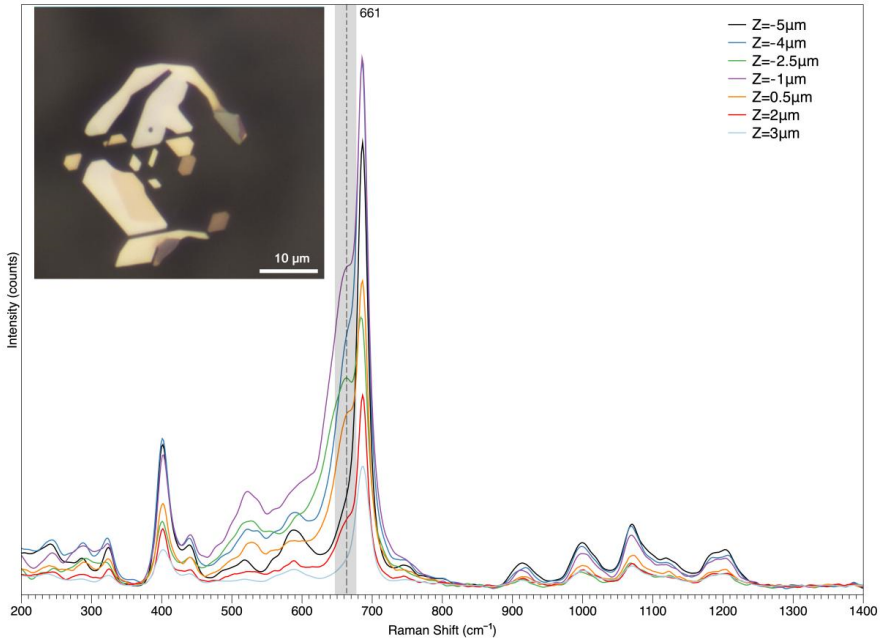

Figure 9. One magnetite was selected for Raman mapping. This figure demonstrated the strength variation in a 661 cm^{-1} peak along the *z*-axis, ranging from −5 µm to 3 µm with fixed x and y, selecting the 661 cm^{-1} peaks as the indicative peak of magnetite.

The recorded 3D mapping image results are illustrated in Figure 10, where the legend bar indicates the intensity of the selected prominent Raman peak with specific colors. For example, orange designates a weak signal of 661 cm^{-1}, while other colors are in between,

and red denotes a strong signal. As a result, the color change caused by the magnetite's primary peak intensity can be used to illustrate the mineral's morphology. As shown in Figure 10, the images explicate the outline shape of the platy magnetite. More importantly, the fluctuation in the magnetite's primary peak may be a valuable tool for deciphering the magnetite's growth process within the gem host. Based on the images and *z*-axis testing range, this magnetite inclusion thickness can be estimated as less than 8 µm.

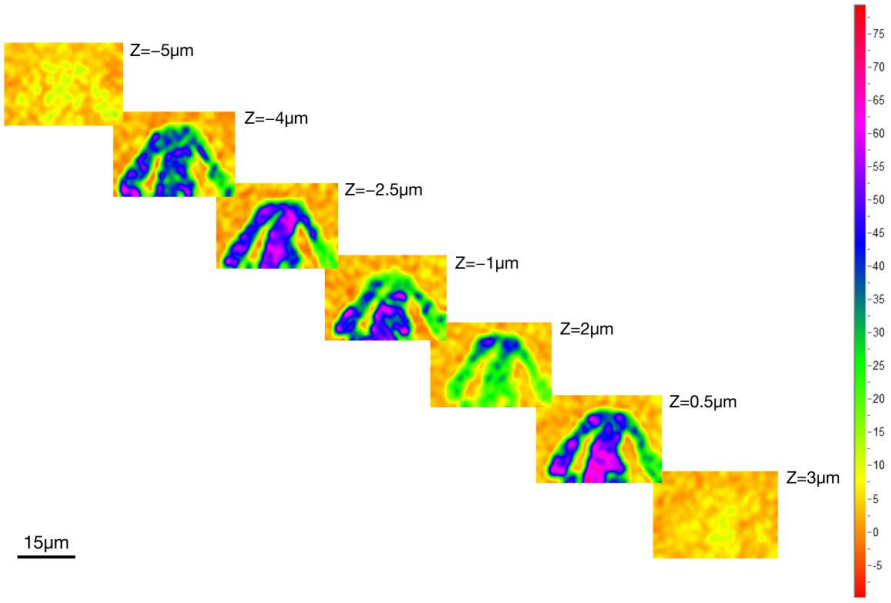

Figure 10. The 3D Raman mapping images show the variation in the strength of the 661 cm^{-1} peaks, outlining the magnetite's shape.

Furthermore, a 3D image of magnetite was generated based on the 661 cm^{-1} peaks, as shown in Figure 11, within a restricted cuboid area. Moreover, the length, width, and height are 31 µm, 15.7 µm, and 12 µm, respectively, forming a three-dimensional volume of 5840.4 $µm^3$. This image demonstrates the distribution and the overall morphology of the magnetite inclusion. The animation allows the viewer to see the inclusions from different angles, usually prohibited by microscopic observation.

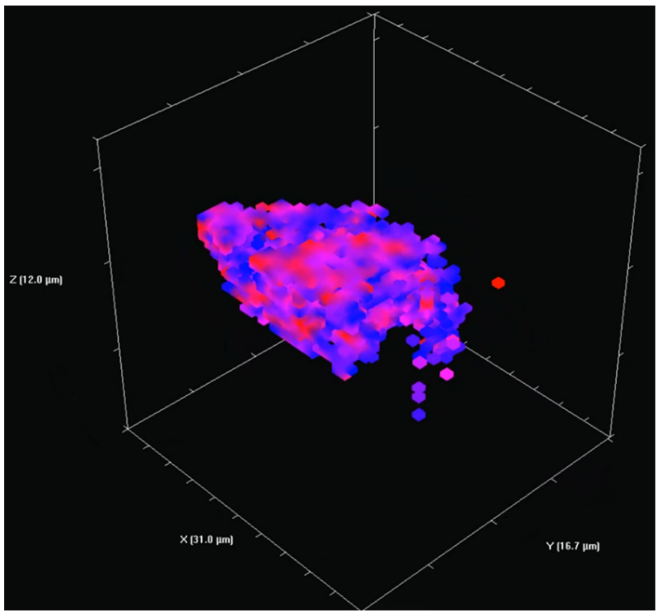

Figure 11. The 3D model of the chosen magnetite was generated based on the 3D Raman mapping, selecting 661 cm^{-1} as a criterion.

3.1.2. Hematite

Hematite is another iron oxide mineral with a chemical formula of Fe_2O_3. In this study, the naked eye barely sees the hematite inclusions. Unlike the concentrated and evenly dispersed magnetite, hematite does not contribute to the trapiche-pattern of the emeralds host. However, many brownish-red colored platy metallic inclusions are also visible under a microscope. They generally showed inhomogeneous size, with their width ranging from 20 to 200 µm, as indicated in Figure 12.

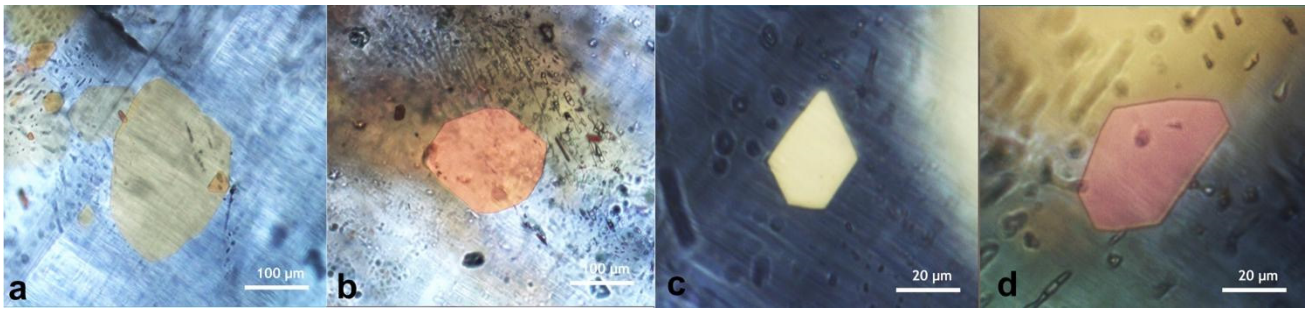

Figure 12. Platy hematite was observed in the gem host, showing subhedral (**a**,**b**) to euhedral (**c**,**d**) hexagonal crystal habit with a yellow to brown color.

Further Raman tests identified them as hematite. As seen in Figure 13, Raman spectrum analysis identifies the large, brownish-red platy inclusion as hematite. It has two feature peaks at 225 and 290 cm^{-1}, weak peaks at 407, 495, 607, and 658 cm^{-1}, and a prominent broad, centered at 1310 cm^{-1}, all of which agree with the main peaks of hematite from the RRUFF online database.

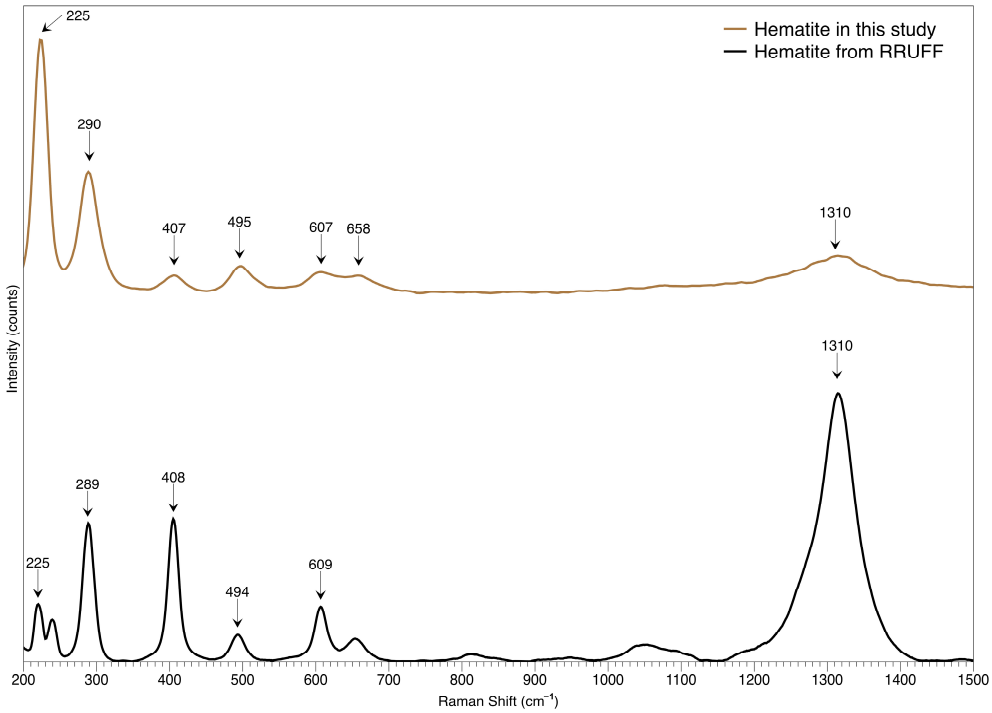

Figure 13. Raman spectrum analysis identifies the large and brownish-red platy inclusion as hematite, with two feature peaks at 225 and 290 cm^{-1} and small peaks at 407, 495, 607, and 658 cm^{-1}, and a prominent broad centered at 1310 cm^{-1}, agreeing with the main peaks of hematite from the RRUFF online database.

The 3D Raman mapping was conducted on one selected plate to further study the hematite's morphology. Figure 14 contains seven Raman spectra recorded on this chosen hematite with a constant *z*-axis value ranging from −48 µm to 48 µm with fixed x and y, as indicated by the legend. The intensity of the feature peak of hematite at 1310 cm^{-1} starts to increase as the Z value starts from −48 µm, and it became most distinct when z = 0 µm, and decreased to nearly none at the z value moved to 48 µm.

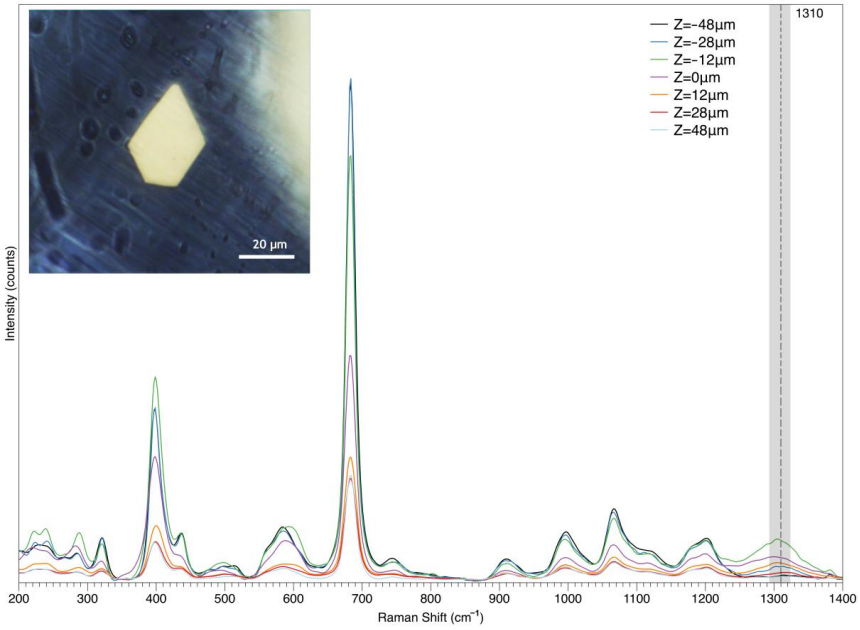

Figure 14. One hematite was selected for Raman mapping, and this figure demonstrated the strength variation in the 1310 cm^{-1} peak along the *z*-axis, ranging from −48 µm to 48 µm with fixed x and y.

The 3D Raman mapping images in Figure 15 demonstrated the hematite plate's hexagonal shape based on the variation in the strength of the 1310 cm^{-1} peaks of the chosen hematite in Figure 14, with fixed x and y, while the Z value ranged from −48 µm to 48 µm. The thickness of this hematite plate is much thicker than the magnetite, nearly 96 µm. A 3D model of the selected hematite was reconstructed based on the 3D Raman mapping, selecting 1310 cm^{-1} as a criterion, as shown in Figure 16.

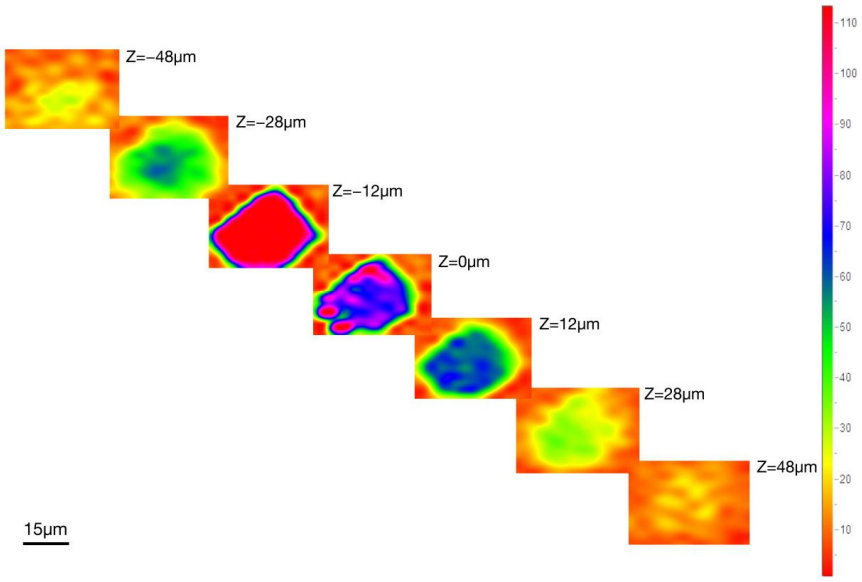

Figure 15. The 3D Raman mapping images show the variation in the strength of the 1310 cm^{-1} peaks, outlining the hematite's shape.

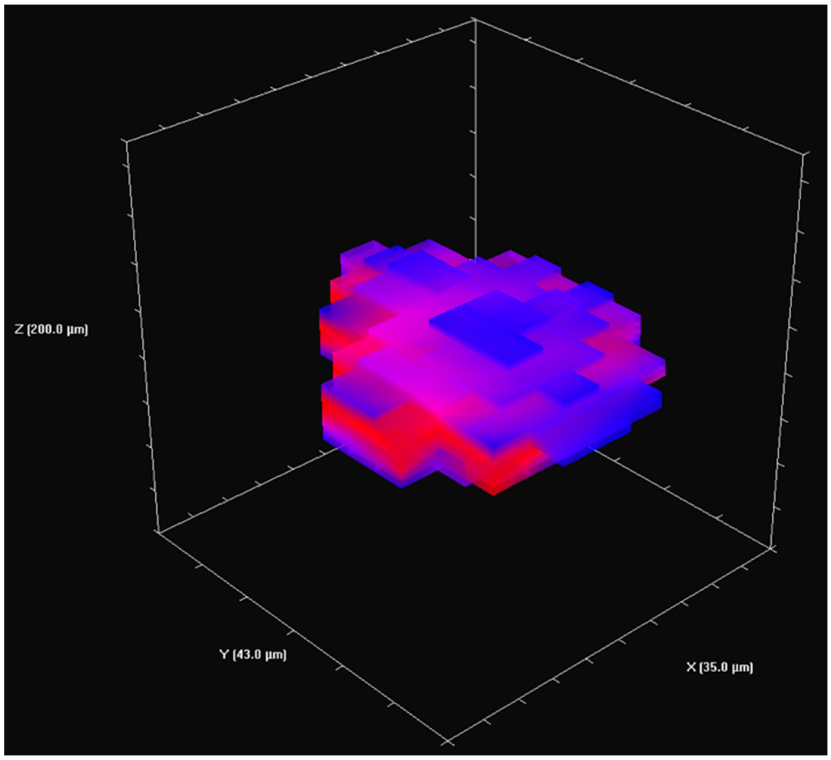

Figure 16. The 3D model of the selected hematite was reconstructed based on the 3D Raman mapping, selecting 1310 cm^{-1} as a criterion.

HXRCT imaging reveals the overall distribution of all the metallic inclusions, as seen in Figure 17 At the same time, the Raman spectrum identifies the metallic inclusions as magnetite and hematite, creating a 3D image of the carefully specified platies. Post-processing software calculation reveals a 0.07% volume proportion regarding the host. Although they seem to be generally uniformly distributed, the layer-by-layer scanning result shows a fluctuating proportion ranging from 0.02% to 0.15%, with an average value of 0.07%, as shown in Figures 17 and 18.

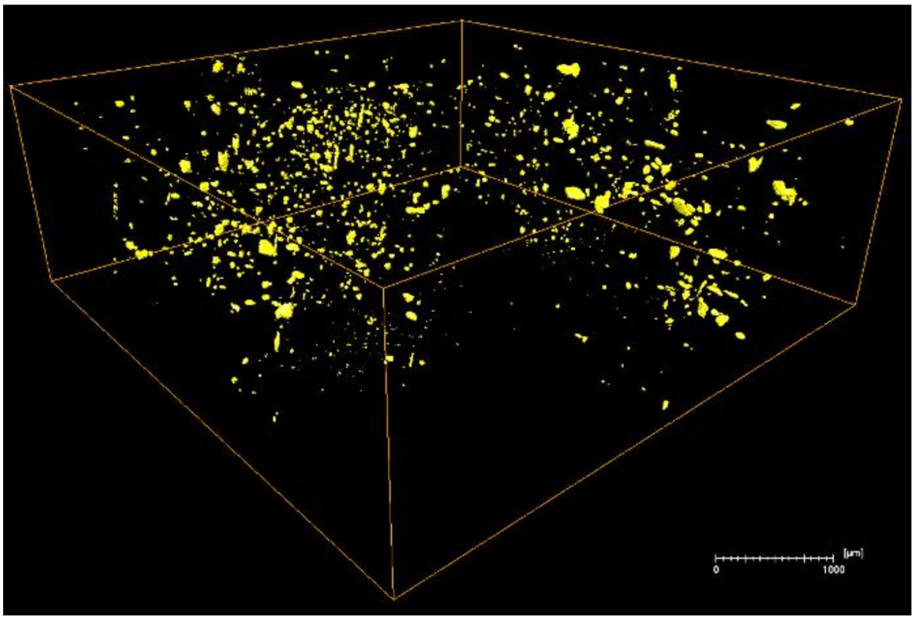

Figure 17. The HRXCT images show that the metallic inclusions distribute relatively uniformly and take up 0.07% volume of the host.

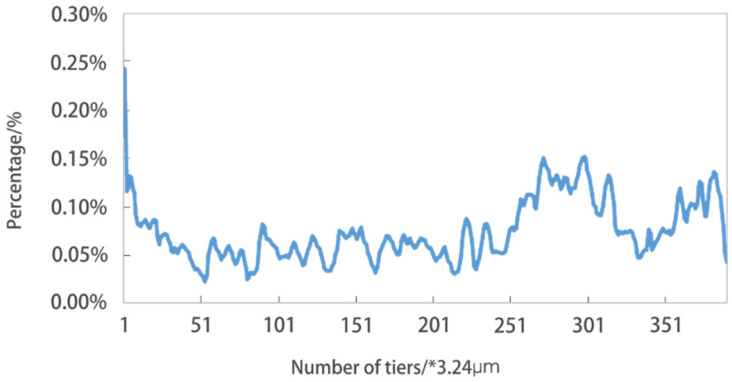

Figure 18. Diagram of volume proportion change in the metal minerals along the direction of sample thickness.

3.2. The Voids

Among the host, numerous tiny voids were observed, filled with multiple phases, as shown in Figure 19. Most of the voids showed a flattened shape parallel to the (0001) basal face with an irregular or elongated outline (Figure 20). Raman tests identify the phases as a mixture of CO_2 and N_2, with two prominent peaks at 1280 and 1386 cm^{-1} assigned to CO_2 and one strong peak at 2328 cm^{-1} attributed to N_2 (Figure 21). The movability of these fluids prohibits further 3D Raman mapping.

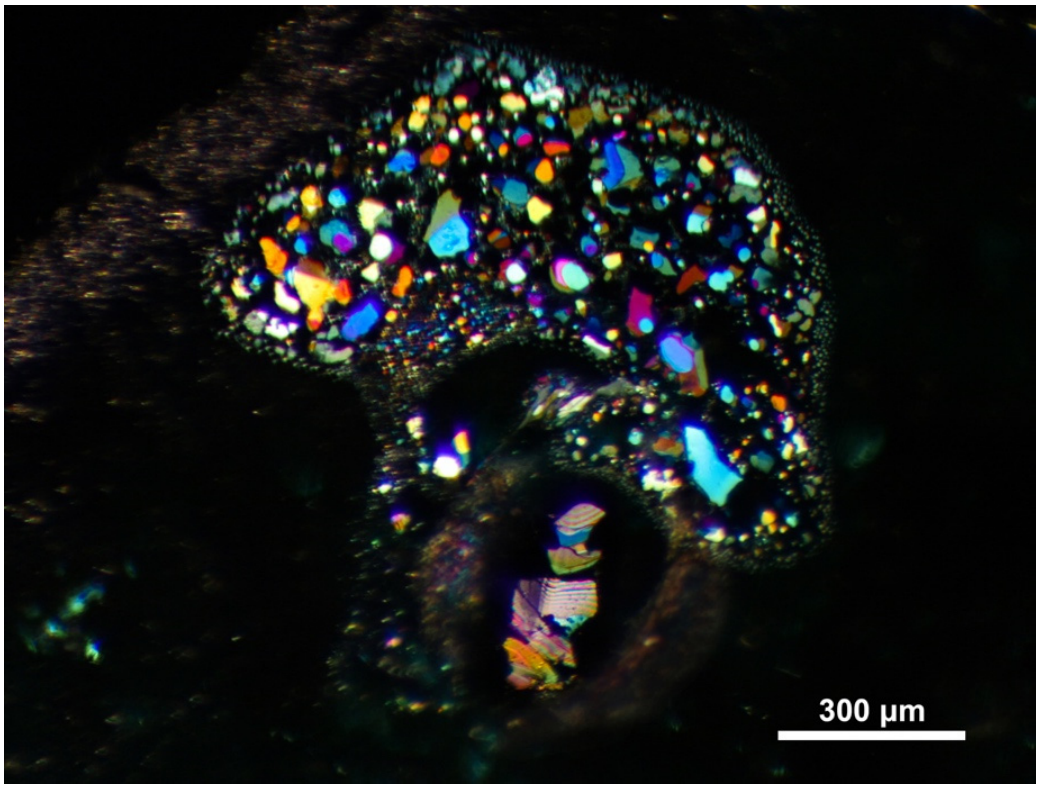

Figure 19. The thin film consists of minute voids that show distinct interference color under microscopic observation.

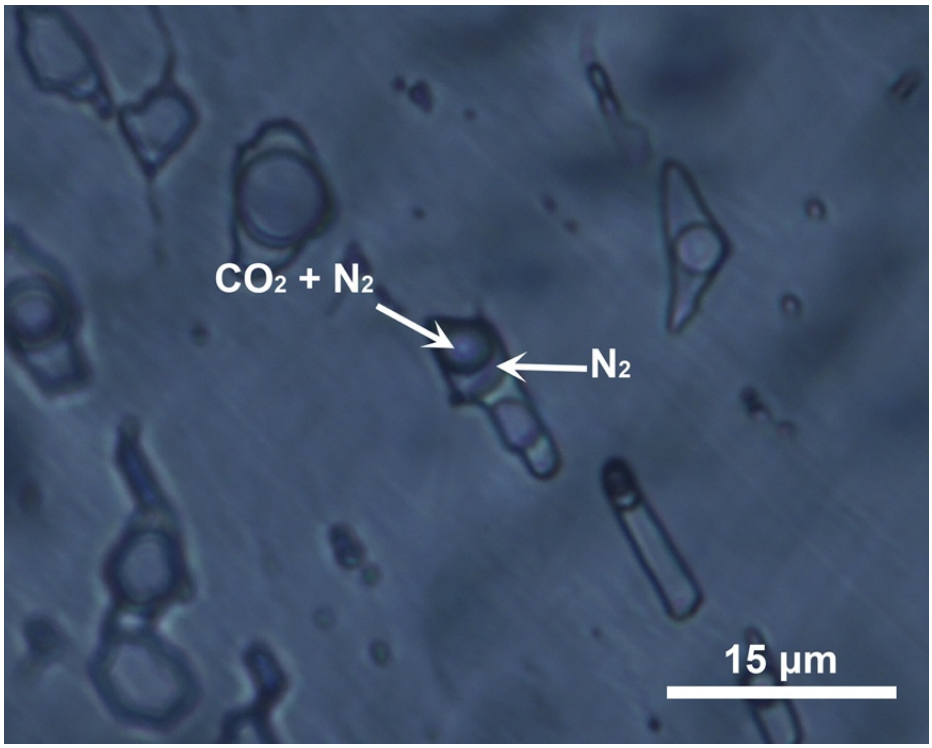

Figure 20. Minute tiny voids were observed filled with fluid inclusions.

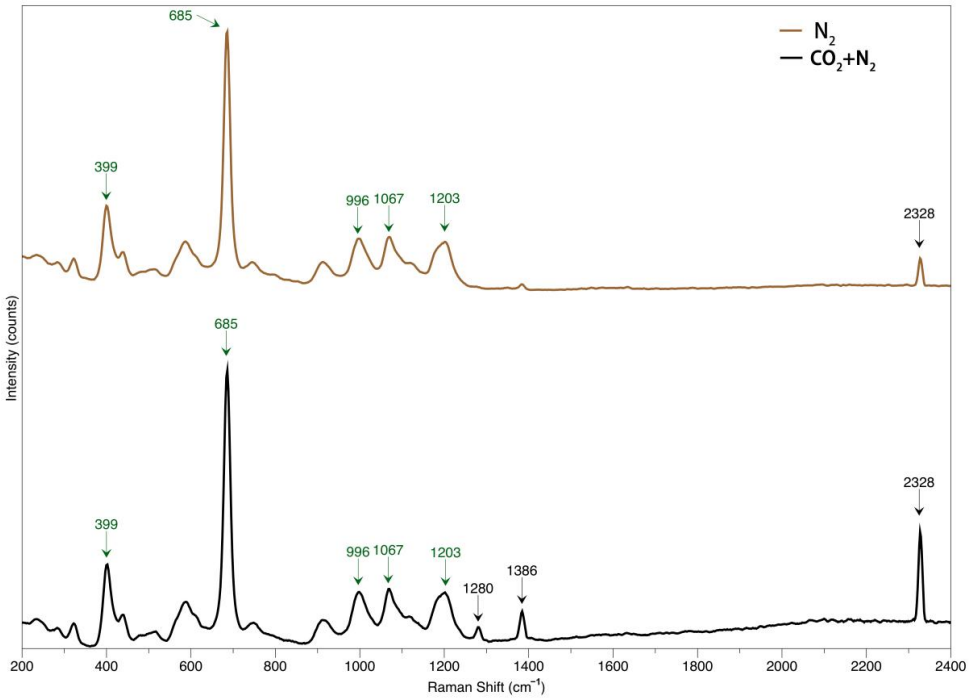

Figure 21. Raman spectrum detected CO_2 and N_2 within the voids, with prominent peaks at 1280 and 1386 cm^{-1} and at 2328 cm^{-1}, respectively.

The HRXCT test showed a continuous change in the volume proportion change of the voids along the direction of sample thickness, as shown in Figure 22. While a distinct fluctuation occurs between the range of 251–301 tiers, indicating large internal fractures in this area, most of the voids vary between 0.01% and 0.05%, taking up 0.03% of the gem host by volume, on average (Figure 23). These HRXCT results proved useful in forecasting internal fracture, usually unseen by microscopic observation.

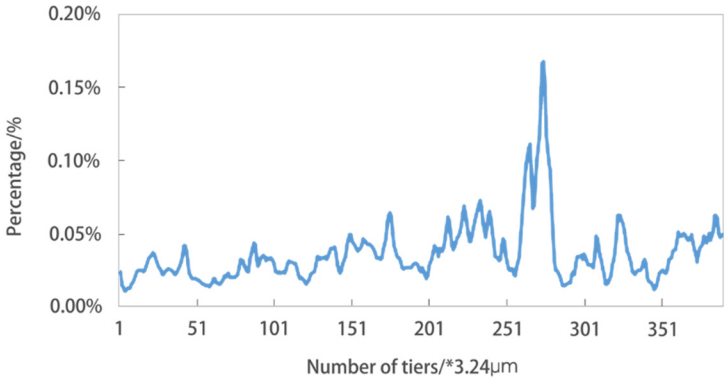

Figure 22. Diagram of volume proportion change in the voids along the direction of sample thickness.

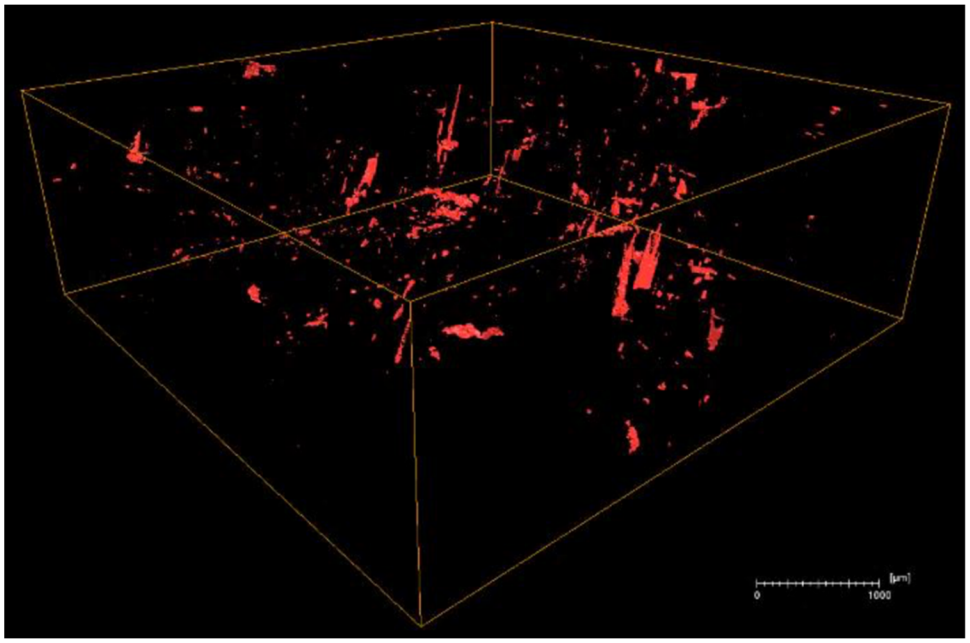

Figure 23. The HRXCT images show the void distribution as relatively uniform, and they take up 0.03% volume of the host, on average.

3.3. The Hexagonal Core

The X-ray image shows the core with a nearly regular hexagonal shape (Figure 24). The size measurement shows that the side length of the hexagon is approximately 0.671 mm, and the distance between parallel side lengths is 1.140 mm. The internal angle is 121.298 degrees, very close to the standard inner angle of the hexagonal crystal system mineral. The deviation in the inner angle value can be attributed to the position of the sample wafer, which is precisely cut and polished to position the C-axis of the emerald host perpendicular to the wafer planes. Based on the value of the side length and the inner angle, the area of the hexagonal cross-section is approximately 3.49 mm^2. Further calculation based on the value acquired provides the volume of the core. As the scanning continues along the direction of sample thickness, the volume proportion varies slightly, but no distinct fluctuation is observed.

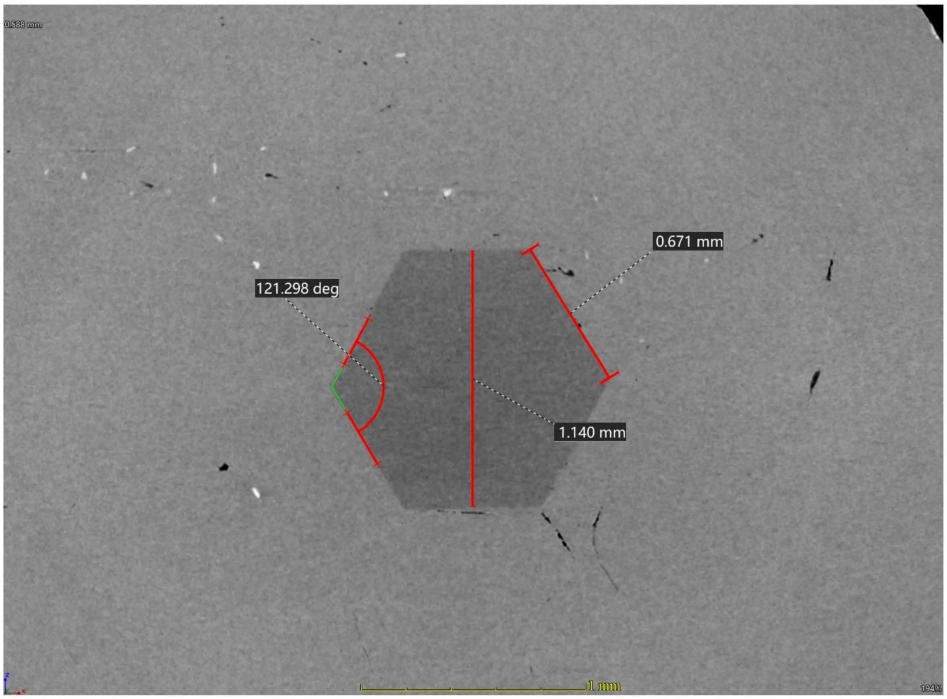

Figure 24. Measurement of the hexagonal core shows an internal angle of 121.298 degrees, a side length of 0.671 mm, and a distance between two parallel sides of 1.140 mm.

The volume proportion change in the core is relatively stable compared with the voids and metal inclusion (Figure 25), suggesting that the center is a well-formed hexagonal crystal. Furthermore, the final result showed that the core takes up approximately 8.25% of the host by volume, on average (Figure 26). Again, the volume proportion could be even more stable and less deviated if the wafer is cut perpendicular to the c-axis.

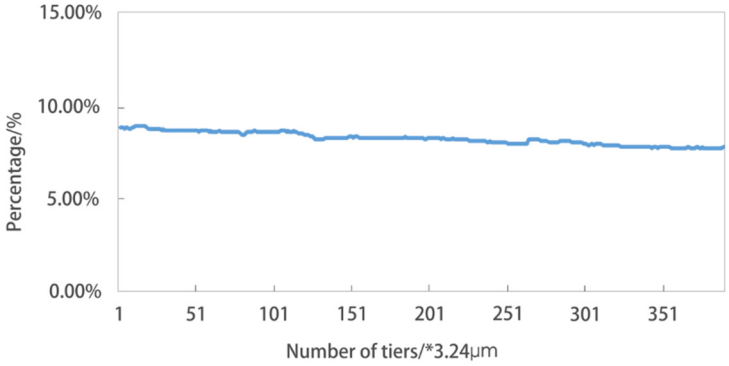

Figure 25. Diagram of volume proportion change in the hexagonal core along the direction of sample thickness.

The color variations in Figure 26 indicate that the core and the emerald host possess different densities, since the CT image shows different colors. It is worth pointing out that no distinct gemological feature variations were observed in the current state, such as the luster and R.I.

Further Raman testing was performed on the core, and the recorded spectrum shows peaks at 685 cm^{-1} and 399 cm^{-1}, which agrees with beryl (Figure 27). Further line mapping with 10 selected points from the host to the center was carried out. The Raman spectrum of the core agrees with the emerald host very well, and no distinct spectrum features' variations were found between the host and the core, as shown in Figure 27.

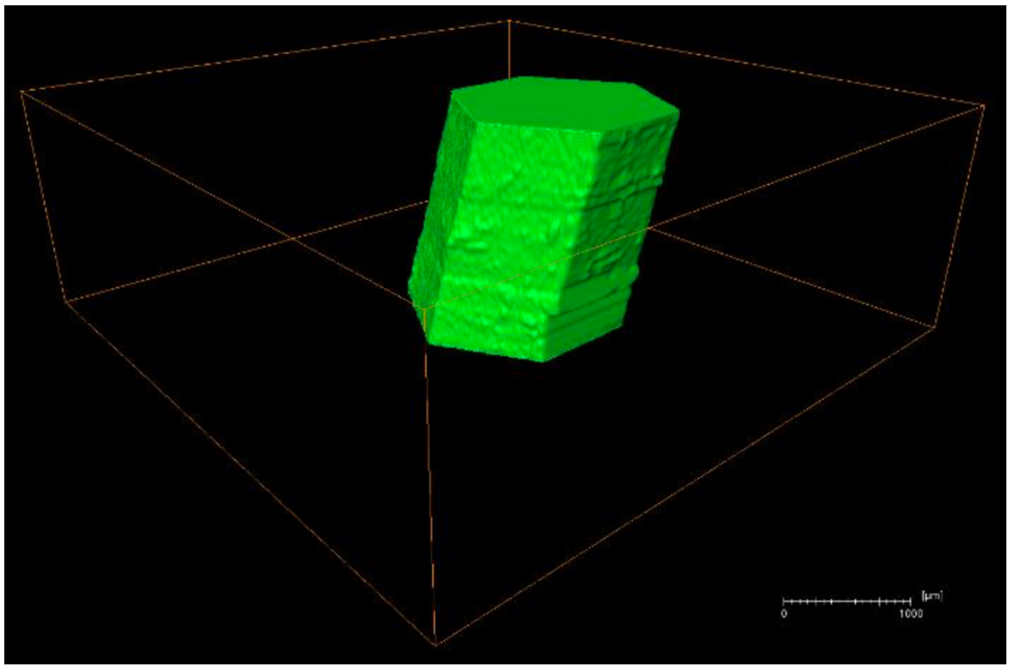

Figure 26. The HRXCT image shows the core as a well-formed hexagonal prism, which takes up 8.25% volume of the host.

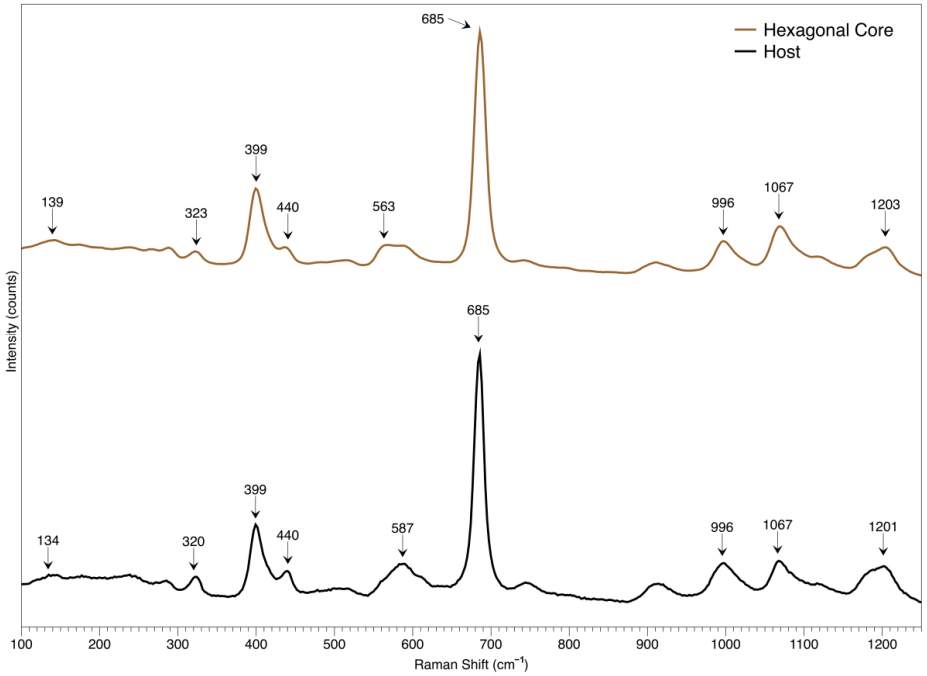

Figure 27. Raman spectrum identified the core as beryl, consistent with the emerald host.

The core may be the starting crystal seed, which crystallized previous to the emerald host, with insufficient trace elements to produce a prominent green color. Further study will focus on the crystalline relationship between the emerald host and metallic minerals.

When considering the distribution of fluid, minerals, and the core within the emerald host, a whole structure was reconstructed three-dimensionally (Figure 28).

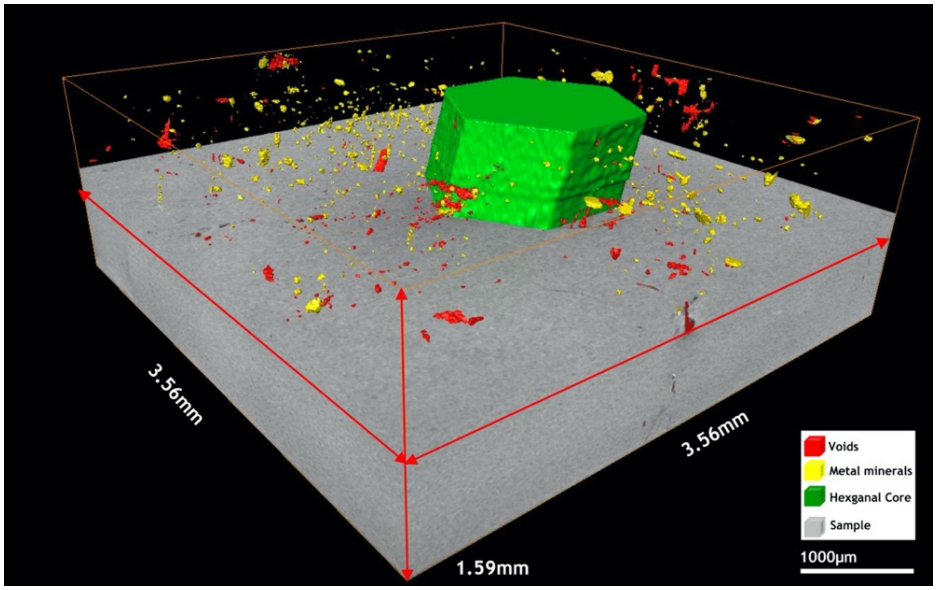

Figure 28. The reconstructed images demonstrated the distribution of fluid, minerals, and the core within the emerald host in a three-dimensional way.

4. Conclusions

The inclusion study has been a significant subject in gemology, which helps identify the gem, detect the treatment, and provide geographic information. Standard gemological microscopic observation enables us to see the inclusion. Further, Raman microscopy proves to be an efficient technique to identify the inclusion without damaging the stone. These three techniques cover the visual, spectral, and structural perspectives. Their combination could serve as a comprehensive solution to study the inclusion of gemstones.

A seasoned cutter usually performs the cutting process to maximize the rough gem value in color, clarity, and weight. Any large fractures or undesired inclusion may cause damage to the gem, thus, decreasing the value or even eliminating the whole stone. Hence, the scanning by high-resolution X-ray CT can provide much more information on the distribution of inclusions and fractures within the rough, which is barely known to a cutter.

Lastly, high-quality and large-sized colored stones, such as ruby, blue sapphire, and emerald, are usually highly valued. This combined technique may further provide unique information from the notable inclusion within the stone. Such information is very critical for the appraiser and auction house. Moreover, even when the stones are mounted or recut, the inclusion information generated by Raman mapping and CT is still valid as the interior features remain untouched.

Author Contributions: Conceptualization Y.G., M.H. and X.L.; methodology, Y.G., M.L, X.S. and Y.Z.; software, X.S. and Y.Z.; validation, Y.G. and M.H.; formal analysis, Y.G.; investigation, M.L. and X.L.; resources, M.H. and X.L.; data curation, Y.G. and M.H.; writing—original draft preparation, Y.G.; writing—review and editing, M.H., M.L. and X.S.; visualization, Y.G.; supervision, Y.G.; project administration, Y.G. and M.L.; funding acquisition, M.H. All authors have read and agreed to the published version of the manuscript.

Funding: This research was funded by the National Science and Technology Infrastructure, The National Infrastructure of Mineral, Rock and Fossil Resources for Science and Technology (http://www.nimrf.net.cn, accessed on 25 December 2021), and the Program of the Data Integration and Standardization in the Geological Science and Technology from MOST, China, grant number 2013FY110900-3.

Acknowledgments: Han Qi and Deng Kaiyin are thanked for their help with the Raman test and photographing.

Conflicts of Interest: The authors declare no conflict of interest.

References

1. Gao, Y.; Sun, X. Uncover the Internal World of Gemstones Part II: Formation and Classification. *Gemol. Front.* **2020**, *1*, 211–226.
2. Palke, A.C.; Saeseaw, S.; Renfro, N.D.; Sun, Z.; McClure, S.F. Geographic Origin Determination of Ruby. *Gems Gemol.* **2019**, *55*, 580. [CrossRef]
3. Zwaan, J.C. Emeralds from the Kafubu area, Zambia. *Gems Gemol.* **2005**, *41*, 116–148. [CrossRef]
4. Saeseaw, S.; Renfro, N.D.; Palke, A.C.; Sun, Z.; McClure, S.F. Geographic Origin Determination of Emerald. *Gems Gemol.* **2019**, *55*, 614. [CrossRef]
5. Kaminsky, F.V.; Wirth, R.; Morales, L. Internal texture and syngenetic inclusions in carbonado. *Can. Miner.* **2013**, *51*, 39–56. [CrossRef]
6. Koivula, J.I. Useful Visual Clue Indicating Corundum Heat Treatment. *Gems Gemol.* **2013**, *49*, 39. [CrossRef]
7. Raman, C.V.; Krishnan, K.S. Polarisation of Scattered Light-quanta. *Nature* **1928**, *122*, 169. [CrossRef]
8. Bersani, D.; Lottici, P.P. Applications of Raman spectroscopy to gemology. *Anal. Bioanal. Chem.* **2010**, *397*, 2631–2646. [CrossRef]
9. Palanza, V.; Di Martino, D.; Paleari, A.; Spinolo, G.; Prosperi, L. Micro-Raman spectroscopy applied to the study of inclusions within sapphire. *J. Raman Spectrosc.* **2008**, *39*, 1007–1011. [CrossRef]
10. Fritsch, E.; Gaillou, E.; Ostrooumov, M.; Rondeau, B.; Devouard, B.; Fritsch, E.; Gaillou, E.; Ostrooumov, M.; Rondeau, B.; Devouard, B. Relationship between nanostructure and optical absorption in fibrous pink opals from Mexico and Peru. *Eur. J. Mineral.* **2004**, *16*, 743–752. [CrossRef]
11. Krzemnicki, M.S. Diopside Needles as Inclusions in Demantoid Garnet From Russia: A Raman Microspectrometric Study. *Gems Gemol.* **1999**, *35*, 192–195. [CrossRef]
12. Kiefert, L.; Karampelas, S. Use of the Raman spectrometer in gemmological laboratories: Review. *Spectrochim. Acta Part A Mol. Biomol. Spectrosc.* **2011**, *80*, 119–124. [CrossRef]
13. Eaton-Magaña, S.; Breeding, C.; Palke, A.; Homkrajae, A.; Sun, Z.; McElhenny, G. Raman and Photoluminescence Mapping of Gem Materials. *Minerals* **2021**, *11*, 177. [CrossRef]
14. Johnson, M.L. Technological developments in the 1990s: Their impact on gemology. *Gems. Gemol.* **2000**, *36*, 380–397. [CrossRef]
15. Sunagawa, I.; Yasuda, T.; Fukushima, H. Fingerprinting of two diamonds cut from the same rough. *Gems. Gemol.* **1998**, *34*, 270–280. [CrossRef]
16. Diehl, R.; Herres, N. X-ray Fingerprinting Routine for Cut Diamonds. *Gems Gemol.* **2004**, *40*, 40–57. [CrossRef]
17. Karampelas, S.; Michel, J.; Zheng-Cui, M.; Schwarz, J.-O.; Enzmann, F.; Fritsch, E.; Leu, L.; Krzemnicki, M.S. X-ray Computed Microtomography Applied to Pearls: Methodology, Advantages, and Limitations. *Gems Gemol.* **2010**, *46*, 122–127. [CrossRef]
18. Krzemnicki, M.S.; Friess, S.D.; Chalus, P.; Hänni, H.A.; Karampelas, S. X-ray Computed Microtomography: Distinguishing Natural Pearls from Beaded and Non-Beaded Cultured Pearls. *Gems Gemol.* **2010**, *46*, 128–134. [CrossRef]
19. Cnudde, V.; Boone, M.N. High-resolution X-ray computed tomography in geosciences: A review of the current technology and applications. *Earth-Sci. Rev.* **2013**, *123*, 1–17. [CrossRef]
20. da Costa, M.F.; Kyle, J.R.; Lobato, L.M.; Ketcham, R.A.; e Silva, R.C.F.; Fernandes, R.C. Orogenic gold ores in three-dimensions: A case study of distinct mineralization styles at the world-class Cuiabá deposit, Brazil, using high-resolution X-ray computed tomography on gold particles. *Ore Geol. Rev.* **2021**, *140*, 104584. [CrossRef]
21. Giuliani, G.; Boiron, M.C.; Morlot, C.; Raoul, J.; Chatagnier, P.Y. Demantoid garnet with giant fluid inclusion. *Gems. Gemology.* **2015**, *51*, 4.
22. Richard, A.; Morlot, C.; Créon, L.; Beaudoin, N.; Balistky, V.S.; Pentelei, S.; Dyja-Person, V.; Giuliani, G.; Pignatelli, I.; Legros, H.; et al. Advances in 3D imaging and volumetric reconstruction of fluid and melt inclusions by high resolution X-ray computed tomography. *Chem. Geol.* **2019**, *508*, 3–14. [CrossRef]
23. Heyn, R.; Rozendaal, A.; Du Plessis, A.; Mouton, C. Characterization of Coloured Gemstones by X-ray Micro Computed Tomography. *Minerals* **2021**, *11*, 178. [CrossRef]
24. Bertrand, E. Compterendu de la séance du 13 Février 1879 Report of the meeting of February 13, 1879. *Bull. Soc. Minéral. Fr.* **1879**, *2*, 31.
25. Pogue, J.E. The emerald deposits of Muzo, Colombia. *Trans. Am. Inst. Min. Eng.* **1916**, *55*, 383–406.
26. Pignatelli, I.; Giuliani, G.; Ohnestetter, D.; Agrosì, G.; Mathieu, S.; Morlot, C.; Branquet, Y. Colombian Trapiche Emeralds: Recent Advances in Understanding Their Formation. *Gems. Gemol.* **2015**, *51*, 222–259. [CrossRef]
27. Gao, Y.; Sun, X.; Shan, M. Trapiche emerald from Swat Valley, Pakistan. *Gems Gemol.* **2019**, *55*, 441–442.